geosciences

MDPI

Article

Physical Parameters and Contrasts of Wooden Objects in Lacustrine Environment: Ground Penetrating Radar and Geoelectrics

Annika Fediuk *, Dennis Wilken, Tina Wunderlich and Wolfgang Rabbel

Institute of Geosciences, Christian-Albrechts-University of Kiel, Otto-Hahn-Platz 1, 24118 Kiel, Germany; dennis.wilken@ifg.uni-kiel.de (D.W.); tina.wunderlich@ifg.uni-kiel.de (T.W.); wolfgang.rabbel@ifg.uni-kiel.de (W.R.)

* Correspondence: annika.fediuk@ifg.uni-kiel.de

Received: 10 February 2020; Accepted: 14 April 2020; Published: 16 April 2020

Abstract: We investigate how suitable ground penetrating radar (GPR) and geoelectrics are to prospect the remains of submerged wooden archaeological constructions in the water column. For this purpose, we determined the contrasts of electric resistivity and dielectric permittivity from measurements on present-day wood samples, serving as simplified approximations of water saturated and undegraded archaeological wood. As common substitutes of hard and soft construction wood, we investigated oak and spruce wood. The electric resistivity and dielectric permittivity were determined with increasing moisture content from small-scale electric and GPR measurements using a Wenner alpha array and a 2 GHz Palm antenna in a watering experiment. In a water-saturated state, resistivity values of <270 Ωm and relative dielectric permittivity values of >20 were observed. The anisotropy effects and deviations of the wood species were seen to be up to 30%. On the basis of this, the relative material contrasts of wood with respect to fresh water, sand, and clay were calculatedand compared to values found in the literature for seismic contrasts. Geoelectric, GPR, and seismic measurements show contrasts of 0.3 to 0.8, −0.4 to 0.2, and −0.24 to 0.35, depending on the surrounding material and structural orientation of the wood. The highest contrasts were found for wood in fresh water, followed by clayey and sandy subsoils. On the basis of the determined contrasts, analytical calculations were performed showing that an object of 0.5 m diameter can be detected at depths between 0.5 m and 1.5 m with geoelectrics (Schlumberger) and at depths between 0.5 m and 3 m with ground penetrating radar measurements (400 MHz).

Keywords: wood; geoelectrics; ground penetrating radar; material contrasts; archaeological prospection; freshwater

1. Introduction

In recent years, the geophysical prospection of archaeological targets has been extended to amphibious terrains and shallow water environments. Current research issues include prospecting anthropogenic harbor installations [1–3] and geoarchaeological indications of harbor environments [4,5], as well as archaeological objects submerged due to sea-level variations or river relocations [6]. A major construction material used in the past was wood, which was used for building ships, buildings, jetties, etc. Using locally available wood species, wooden buildings in Central Europe were often made of oak. Conifers were used in Scandinavia. The properties of individual wood species were used for specific components, e.g., of ships. Thus, ship wrecks often consist of a variety of hard and soft woods [7–9]. In onshore archaeological prospection, five geophysical methods are well established: magnetics, seismics, electromagnetic induction (EMI), geoelectrics (mostly electric resistivity tomography (ERT)),

and ground penetrating radar (GPR). In offshore environments, mostly hydro-acoustic/seismic methods are used [10]. Here, the contrasts of woods have been intensively studied. In [11], the seismic reflection coefficients of wood in different weathering grades were calculated. They show large differences in the reflection coefficients, caused by the weathering degree and the subsoil. Therefore, with seismic methods, wooden archaeological remains can sometimes be detected excellently, sometimes not. As an example, it is hard to prospect moderately degraded oak in clay. However, seismic methods can be complemented or replaced by ERT and GPR measurements. We recognized the potential of lacustrine GPR to image small-scale wooden structures from a sample profile showing multiple reflections that come from trunks and branches in the water column. Similar experiences were noted in [12] while searching for submerged lumber with GPR. They recognized diffraction hyperbolas caused by lumber both above and below the lake bottom within organic sediment. ERT and GPR become especially attractive in cases of extremely shallow water and gassy environments. For addressing the material or the degree of preservation of objects, the methods can be used as they are sensitive to lateral and vertical changes in the subsurface electric resistivity and dielectric permittivity. However, the high conductivity of the water column results in a limited depth penetration. In [6,13], ERT studies are presented, and in [14,15], GPR studies are presented investigating submerged nonwooden objects. Their results show that both marine ERT and GPR are suitable methods to resolve objects within the meter scale, e.g., wall fundaments and bombs. In [16], the authors offer an approach to determine subsurface material contrasts based on the GPR signal strengths from sediments and a reference aluminum plate. However, there is no study investigating wooden material contrasts for marine and lacustrine ERT and GPR measurements.

Several studies, summarized in [17–19], investigated the electric resistivity and dielectric permittivity of wood with increasing wood moisture content. In [20,21] among others, it is observed that there is a decrease in the electric resistivity with increasing wood moisture. In [22], the effects of fiber orientation are considered. However, most studies focus on wood moisture contents of 0%–30%, which do not represent the higher moisture content expected in archaeological wood [23]. An increase in permittivity is noted, for example, in [24]. They investigated spruce wood for different measurement frequencies (in both the MHz and GHz range) and wood-moisture contents. In [25], they carried out similar investigations for Douglas fir. In [26], they considered the influence of fiber direction on the dielectric permittivity of dry wood. However, especially for fully water-saturated wood, which is comparable to archaeological wood, the studies do not cover all aspects regarding the influence of structural orientation and the distinction between oak as a hardwood and spruce as a softwood. In addition, the electrical resistivity of wood is usually determined using a resistance meter with two electrodes [19]. The dielectric permittivity is determined using plate capacitors [17]. Thus far, none of the studies have used small-scale geophysical methods such as geoelectric four electrode arrays and GPR antennas for that purpose. Therefore, in this study, we bride this gap and investigate to what extent ERT and GPR are suitable to prospect the remains of submerged or wooden constructions in the water column with respect to physical material parameter contrast. We follow the approach asking whether wood can be detected based on the assumption that modern water-saturated wood is comparable to unweathered archaeological wood. Using this assumption, we can neglect the manifold properties of archaeological wood, including degradation, which are often unknown during field prospection. For further simplification, we consider oak and spruce wood, two typical representatives of hard and soft wood, showing fundamental structural differences.

Regarding the aforementioned background, our study has three aims:

(i) Investigating electric resistivity and dielectric permittivity of modern oak and spruce wood with increasing water moisture contents considering three directions of anisotropy in a long-term experiment. For this purpose, we used small-scale geophysical equipment and compared the results to previous laboratory studies;

(ii) Calculating the physical material contrasts of wood compared to different embedding materials, such as water, clayey subsoil, and sandy subsoil, for ERT and GPR measurements and comparing them to seismic material contrasts based on the work of [11];

(iii) On the basis of the determined contrasts, we performed analytical calculations to investigate the depth penetration and applicability of the ERT and GPR methods for the prospection of wooden objects in water.

2. Materials and Methods

2.1. Preliminary Considerations to Determine Wooden Material Properties

For the determination of material contrasts of wood in different subsurfaces in the field, certain preliminary considerations are required regarding the variations of water-saturated wood. Therefore, we consider the parameters that influence the electric resistivity and dielectric permittivity which can be observed in the experiment.

Wood is an inhomogeneous, anisotropic, and capillary porous composite material of macro-, micro-, and submicron structure [17–19].

Inhomogeneities result from differences in the raw density, irregular water absorption of wood during the experiment, and anisotropic axes because of different structural orientations, among other things. Differences in the raw density are due to various wood species and due to irregular early and late growth rates in the microstructure. The average kiln-dry density for spruce wood is 0.43 g/cm^3, whereas for oak wood an average value of 0.63 g/cm^3 is defined in [17].

Three anisotropy axes define the macrostructure: (1) in fiber direction; (2) radial; and (3) tangential to the annual rings across the fiber direction (Figure 1). Anisotropy affects both the water absorption process and the investigated physical parameters. Therefore, in the context of the study, integral values of electric resistivity and dielectric permittivity were determined along each of the three main structural directions and for both hard and softwood. Thus, different types of cutting and orientations of objects in the subsurface are taken into account.

Figure 1. Anisotropy axes of wood: (1) in the fiber direction; (2) in the direction across the fiber, radial to the annual rings; (3) in the direction across the fiber, tangential to the annual rings.

The wood moisture absorption can be divided into three different states [17,18]. The kiln-dry state of wood has a 0% wood moisture content. In the fiber saturation state, the microstructure and submicron structure are fully saturated with bound water, showing a wood moisture content between 22% and 35%. We focus on the third state, in which the macrostructure becomes water saturated with free water. The expected maximum wood moisture content of 200% for spruce and of 111% for oak depends on the kiln-dry density and the maximum weight of the fiber-saturated state [17]. The wood moisture content u is the relation of the mass from wet wood m_u to the mass from kiln-dry wood m_d:

$$u = \frac{m_u - m_d}{m_d} * 100\,(\%) \tag{1}$$

Furthermore, we have to expect a faster moisturization of spruce wood than oak wood during the watering process and an irregular expansion of the wooden cell walls until maximum fiber saturation

is reached. In the fiber direction, the swelling rate is <0.5% and in the direction across the fiber, the swelling rate is >5% for both wood species [17].

2.2. Experimental Setup

In the first step, the physical parameters electric resistivity ρ_s and dielectric permittivity ε_r were determined as a function of the wood moisture content u in a nine-month watering experiment. We applied the geophysical methods geoelectrics, using Wenner α resistivity measurements (WA), and GPR, using a 2 GHz antenna in a suitable small-scale setup. The measurements were performed on two $10 \times 10 \times 10$ cm^3 cubes of oak and spruce wood. The measurements were performed on three side surfaces of the cubes corresponding to the main directions of anisotropy along the fiber as well as radially and tangentially to the annual rings across the fiber direction (see Figure 2). The size of the cubes was chosen to fit the geometric demands of the 2 GHz GPR antenna (9.2 cm × 9.2 cm), whereas larger cubes would not be suitable because of the longer moisture saturation time. At the beginning of the experiment, the kilning method described in [17] was used to dry the wood to mass constancy at 103 °C ± 2 °C. The wood cubes were then placed into a tank of fresh water with an average electric resistivity of 19 ± 0.4 Ωm and a temperature of 17 ± 0.7 °C so that thermal conductivity effects could be ignored. At regular intervals, the wooden cubes were weighed and the wood moisture content was determined using the reference mass. This was done first daily, and then weekly, after the gradient of each curve significantly decreased. Additionally, the wooden cubes were measured with a caliper to document the swelling α, which is the expansion of each side of the moisturized cube in relation to those in the kiln-dry state. The cube expansion is required to calculate the dielectric permittivity from GPR measurements. Each measurement was repeated ten times and the Gaussian law of error propagation [27] was used to calculate the statistical error of the wood moisture content u for the first measurement of our experiment in a dry state, for the fiber-saturated state and for the maximum saturated state. In the dry state, the measurement error of the mass from wood results from inaccuracies in the electronic scale of $\Delta m_d = 0.5$ g. For the fiber-saturated as well as for the maximum saturated state, measurement errors result from the drying process of the wood during the one hour (approximately) measuring procedure. The arithmetical average weight difference between the beginning and ending of the measurement was $\Delta m_u = 3$ g in fiber-saturated state and $\Delta m_u = 9$ g in the saturated state. The time series of the wood moisture content u, the swelling α, the density d, as well as the electric resistivity and permittivity were fitted with mathematical functions and compared to previous laboratory studies [17–19]. Obvious options were low-order polynomial functions and (limited) exponential growth, respectively, decay functions, and the sum of an exponential and a polynomial function. After some trials, the increasing wood moisture content u with time t was fitted by the sum of a limited exponential growth and a polynomial function of first order $\mathrm{a} + \mathrm{b} * \mathrm{t} - \mathrm{c} * \mathrm{e}^{-\frac{\mathrm{t}}{\mathrm{d}}}$. The swelling α depending on the wood moisture content u was fitted by a limited growth curve of type $\mathrm{a} - \mathrm{b} * \mathrm{e}^{-\frac{\mathrm{u}}{\mathrm{c}}}$. The correlation coefficients of the fits are of the order of 0.98 in all cases. From the mass of the moisturized wood and the wood cube volumes, the density d was determined and fitted by a linear curve $\mathrm{a} * \mathrm{x} + \mathrm{b}$. Then, the electric resistivity and dielectric permittivity of the woods were examined. As a result of the internal wood structure of the spruce cube, the radial and tangential components in the direction across the fiber could not be clearly distinguished, which is why we expect to obtain average values of anisotropy for the two orthogonal sounding directions for this wood type.

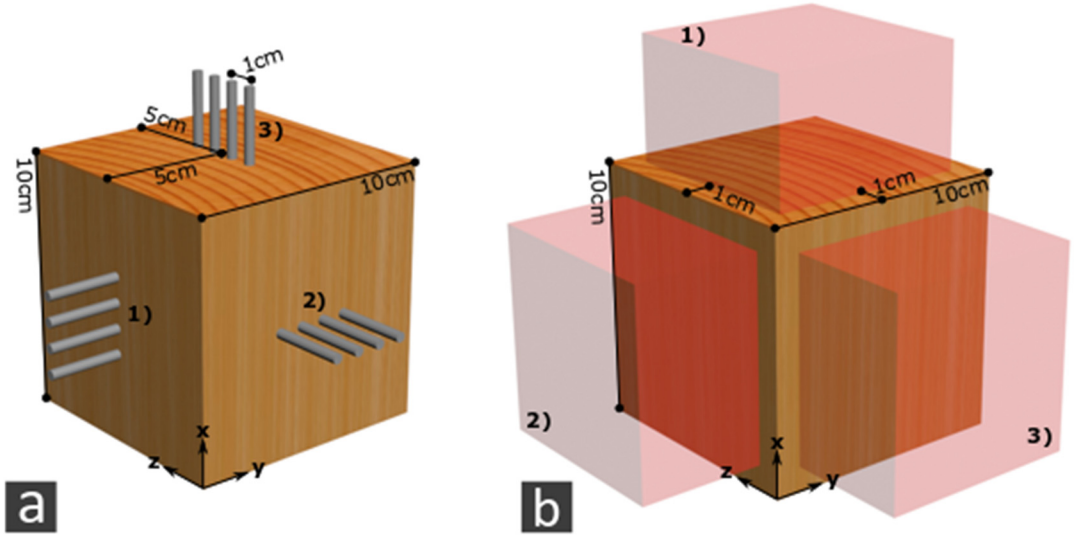

Figure 2. Schematic drawing of: (**a**) the setup for electric resistivity measurements of wood using a Wenner α configuration; (**b**) 2 GHz Palm antenna used for dielectric permittivity measurements of wood. Anisotropy axes of wood are highlighted: (1) in the fiber direction; (2) in the direction across the fiber, radial to annual rings, (3) in the direction across the fiber, tangential to annual rings.

2.3. Determination of the Electric Resistivity

For investigating the electric resistivity of the wood cubes, a four-electrode array made from screws (diameter 1 mm) with a Wenner α configuration of 1 cm electrode distance was centered on three sides of the cube corresponding to the main directions of anisotropy (Figure 2a). The current I and the voltage U were measured with a C.A. 6470 unit (manufactured by Chauvin Arnoux), arithmetically averaging ten repetition measurements. Assuming a homogeneous electric resistivity distribution throughout the block (in the current anisotropy direction), the specific electric resistivity was then defined by Ohm's law [28].

To estimate statistical errors in the dry state, fiber-saturated state, and maximally saturated state (exemplarily for spruce wood in the fiber direction), the Gaussian error law was again applied.

Therefore, errors of the geometry factor $k = 2\pi a = 0.0628$ with an electrode spacing a of 1 cm can be estimated by electrode spacing inaccuracies of 0.1 mm, resulting in an error of $\Delta k = 6.3 \times 10^{-4}$. Measurement errors for the current I [A] and the voltage U [V] were defined as standard deviations from the ten measurement repetitions, and were caused by the resolution accuracy of the registration unit and by errors of the electrode coupling. The measurements could be fitted by a limited exponential decay curve of type $a + b * e^{-\frac{u}{c}}$. To ensure that the measurements were not affected by the boundary surfaces of the $10 \times 10 \times 10$ cm^3 wood cubes, we used the program pyGIMLi [29] to calculate the geometry factor of the Wenner α array for the special situation of a cube, considering the six free surfaces of the probe. This was compared with the geometry factor calculated for the common half-space. To quantify the anisotropy effects in and across the fiber direction, we calculated the relative standard deviations of the arithmetic average of all the measurement directions for each wood moisture content.

2.4. Determination of the Dielectric Permittivity

The relative dielectric permittivity ε_r was determined using a 2 GHz Palm GPR antenna (GSSI) connected to the registration unit SIR 30 (GSSI). The device setup uses two antennas in one housing which cannot be used for transmission but for reflection measurements. The relative dielectric permittivity ε_r is defined by the ratio of the permittivity of a material ε to the permittivity in free space ε_0. It is inversely proportional to the square of the GPR velocity v [30].

We determined ε_r via the radar wave velocity $v = 2s/t$, where s is the side length of the cube and t is the two-way travel time of the radar wave reflected from the cube surface opposed to the side of

the antenna (Figure 2b); t corresponds to the travel time difference between the signal amplitudes of the direct and reflected waves. To enhance the reflection amplitude, we mounted a metal sheet at the bottom of the wooden cube. The metal sheet has a reflection coefficient of −1, which is much stronger than the reflection coefficients of possible internal wood interfaces.

Figure 3a shows that for moisture contents < 20% the travel times of the direct wave and the reflection from the base of the cube are so small that the signals interfere. Consequently, the standard use of first breaks to pick the direct wave (i.e., interference of air and ground wave) and the reflection of the metal sheet is not possible, wherefore we chose to pick the maximum signal amplitude.

To estimate the measurement accuracy in this low moisture range, the experiment was also conducted with a 50 cm long spruce piece of the same log as the 10 cm long piece (Figure 3b). Additionally, this longer piece was used to estimate the inaccuracy that results from picking the first maxima of the wavelets (Figure 3b, option 1, green line) instead of the first breaks (Figure 3b, option 2, yellow line).

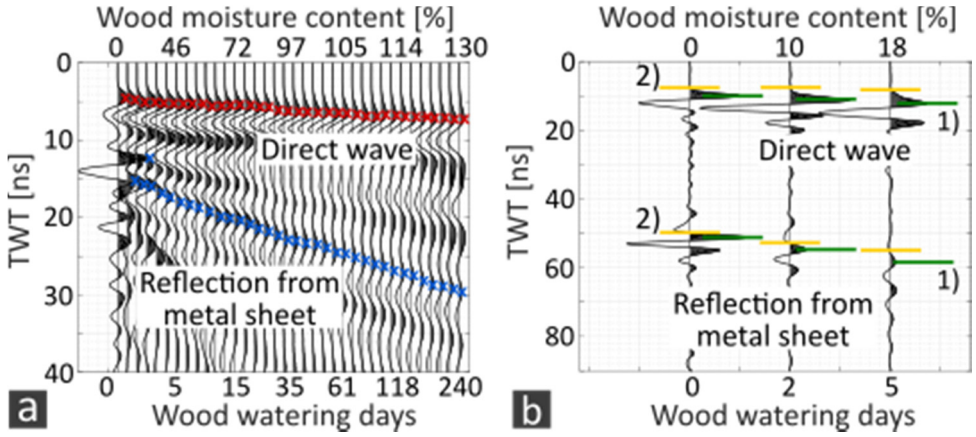

Figure 3. Wiggle plot of spreading corrected radar signals that change with increasing wood moisture content for: (**a**) spruce wood cube of size 10 × 10 × 10 cm^3 in the fiber direction (red and blue marks highlight the picked amplitudes); and (**b**) spruce wood cube of size 10 × 10 × 50 cm^3 in the fiber direction. Here, two possible definitions of the travel time through the wood cubes for kiln-dry and moisturized wood are compared: (1) the maximum signal amplitude from the direct wave respectively wood–metal interface (green); and (2) the zero position before the respective signal amplitude (yellow).

The measurement uncertainties of the GPR measurements were again estimated via the Gaussian error propagation law, considering deviations of the travel time and of the dimensions of the wood. The travel time error Δt = 0.01 ns is defined as the standard deviation of the picked time difference between the signal amplitudes from ten repetition measurements. Errors of the dimensions of the wood cubes Δs = 0.05 cm are caused by inaccuracies using the caliper and an irregular expansion of the wood during the watering process.

The calculated dielectric permittivity values could be fitted by an exponential curve of type $a + b * e^{\frac{u}{c}}$. Anisotropy effects were also considered, using the same approach as for the electric resistivity.

2.5. Determination of Relative Material Parameter Contrasts

In the next step, relative contrasts of the electric resistivity and dielectric permittivity from the submerged wood in three different subsurface materials were determined. Following [11], we selected fresh water, sandy subsoil, and clayey subsoil as the hypothetic embedding materials for the wooden objects.

The parameters for water-saturated oak and spruce wood for three anisotropy directions were taken from the experiment. However, the maximum wood moisture content was not reached by the end of the experiment. Therefore, the values of the electric resistivity and the dielectric permittivity

were extrapolated to the expected maximum wood moisture content using the fitted curves. The parameters of the embedding material were taken from literature and are summarized in Table 1. Especially, saturated sands and clays show a large possible value range, so that exemplary values were chosen for our investigations.

In order to determine the specific resistivity of a sandy subsoil, Archie's law [32] was used assuming a water resistivity of 21 Ωm.

The relative material contrast for the geoelectric measurements depends on the specific electric resistivity of the wood ρ_{sw} and of the subsurface ρ_{ss} [28].

$$r_{\rho_s} = \frac{\rho_{ss} - \rho_{sw}}{\rho_{ss} + \rho_{sw}} \tag{2}$$

Neglecting the influence of the magnetic permeability and the electric resistivity on GPR reflectivity, the effective GPR material contrasts correspond to the reflection coefficients depending on the relative dielectric permittivity of the wood ε_{rw} and of the subsurface ε_{rs} [30].

$$r_{\varepsilon_r} = \frac{\sqrt{\varepsilon_{rs}} - \sqrt{\varepsilon_{rw}}}{\sqrt{\varepsilon_{rs}} + \sqrt{\varepsilon_{rw}}} \tag{3}$$

The relative seismic material contrasts are also equal to the seismic reflection coefficient, depending on the seismic velocity (v_w) and density of the water layer (d_w and of the subsurface layer (v_s and d_s) [28].

$$r_s = \frac{d_s * v_s - d_w * v_w}{d_s * v_s + d_w * v_w} \tag{4}$$

Table 1. Reference values of the electric resistivity and dielectric permittivity for the embedding materials freshwater, saturated sand, and saturated clay.

Embedding Material	Electric Resistivity	Dielectric Permittivity
Freshwater	21 Ωm [31]	81 [31]
Saturated sand	75 Ωm [31,32]	20 [33]
Saturated clay	40 Ωm [34]	40 [33]

2.6. Geophysical Detection Swell of Wooden Targets in Lacustrine Environment

On the basis of the parameter contrasts of wood embedded in soils and freshwater, we finally discuss the implications of the depth range, in which wooden objects can be detected through geoelectric and GPR measurements. This depth detection swell does not only depend on the parameter contrasts but also on the instrumental sensitivity, the ambient noise level, the shape of the objects, and in case of GPR, the attenuation of the up- and downward travelling waves. For this estimate, we assume: (1) that the shape of the wooden objects can be approximated by spheres or long horizontal cylinders oriented orthogonally to the sounding profile; and (2) that the wooden objects are embedded in a homogeneous half space. In these cases, the geoelectrical and GPR ground responses can be estimated analytically. The formulae given below can be derived by simple algebra for GPR from equations provided in [35,36], and the geoelectric sounding in Schlumberger configuration were provided in [37]. Ideal measuring conditions are assumed.

For the geoelectrical detection swell of spheres and horizontal cylinders, we obtained

$$r_{electric\_sphere} = \left(M \frac{\rho_0 + 2\rho_1}{\rho_0 - \rho_1} \right)^{\frac{1}{3}} h_0 \tag{5}$$

and

$$r_{electric\_cylinder} = \left(M \frac{\rho_0 + \rho_1}{\rho_0 - \rho_1} \right)^{\frac{1}{2}} h_0 \quad (6)$$

where $r_{electric\_sphere}$ is the radius of the sphere, $r_{electric\_cylinder}$ is the radius of the cylinder, ρ_0 is the specific resistivity of the half-space, and ρ_1 is the specific resistivity of the sphere/cylinder. h_0 is the midpoint depth of the sphere/cylinder and $z_{top} = h_0$-$r_{electric\_sphere/cylinder}$ is the depth to the top of the object. $M = 2\frac{\Delta\rho_a}{\rho_0}$ is the measurement accuracy within 95% bounds, $\frac{\Delta\rho_a}{\rho_0}$ is the relative standard deviation of the measurements, and ρ_a is the apparent resistivity.

The GPR detection swell of spheres and horizontal cylinders is

$$r_{GPR\_sphere} = \left(P e^{-2\alpha z_{top}} \frac{R}{2 z_{top}} - 1 \right)^{-1} z_{top} \quad (7)$$

and

$$r_{GPR\_cylinder} = \left(P^2 e^{-4\alpha z_{top}} \frac{R^2}{4 z_{top}^2} - 1 \right)^{-1} z_{top} \quad (8)$$

where r_{GPR_sphere} is the radius of the sphere, $r_{GPR\_cylinder}$ is the radius of the cylinder, z_{top} is the depth to the top of the object, P is the GPR system performance, R is the reflection coefficient, and α is the absorption coefficient. We estimated the GPR detection swell for a 400 MHz antenna, which can be used to prospect targets a few meters below the subsurface and is regularly used in the geophysical prospection of archaeological objects. In contrast, the 2 GHz antenna used in the experiment has a depth penetration within the decimeter range and is usually not used during field measurements. However, the experiment could only be carried out using a 2 GHz antenna due to the antenna and wood dimensions. As discussed in Section 4.3.1, dielectric permittivity values increase with lower measurement frequencies. Comparing the frequencies of 400 MHz and 2 GHz, this effect does not significantly change the detection swell. Therefore, we used the measured dielectric permittivity values of the experiment.

The material parameters assumed for the wood and the embedding material, i.e., freshwater, saturated clay, and sand, are listed in Table 2. The technical resolution limits of the field units (electronic noise) and the ambient noise level are critical. For these, we assumed that the geoelectric response of the embedded objects is detectable if it exceeds the background by 2%. For the GPR, we assumed a practical system performance of 96 dB.

Table 2. Summary of the material parameters assumed for the wood and the embedding material, freshwater, saturated clay, and sand to discuss the implications for the depth range.

Geoelectric	Freshwater	Saturated Sand	Saturated Clay
Spec. electric resistivity of half space	21 Ωm	40 Ωm	75 Ωm
Spec. electric resistivity of wood		250 Ωm	
GPR	Freshwater	Saturated sand	Saturated clay
EM wave velocity of half space	3.3 cm/ns	7 cm/ns	5 cm/ns
Attenuation of half space	0.1 dB/m	0.17 dB/m	10 dB/m
Reflection coefficient of wood to embedding material	−0.34	−0.06	−0.17

3. Results

3.1. Water Absorption, Swelling, and Density Increase of Moisturized Wood during the Experiment

Figure 4a shows the development of the wood moisture content for oak u_o (blue) and spruce wood u_s (red) depending on the watering time t of the wood cubes. During the measuring period,

none of the wooden cubes reached their maximum wood moisture content. The experiment was terminated at a final wood moisture content of 100% for oak and of 130% for spruce wood. The increasing wood moisture content for oak wood u_o and spruce wood u_s with time t was approximated by the functions summarized in Table 3. The wood density d shows a linear increase (Figure 4b; for the fitting function see Table 3; for the mean values see Table 4). The swelling of oak α_o and spruce α_s due to an increasing wood moisture content u is shown in Figure 5 across the fiber in radial (a) and tangential directions (b), and in the fiber direction (c). It can be fitted by limited growth curves (Table 3). Directional differences in the swelling are especially apparent in and across the fiber directions. In the fiber direction (Figure 5c), there are only minimal changes of less than 0.5%. In the direction across the fiber, an increase of > 4% was found for oak and spruce wood in the direction across the fiber (radial, Figure 5a; tangential, Figure 5b). The experimentally determined masses, density values, dimensions, and volumes of the wood cubes in kiln-dry and in their maximally saturated state are listed in Table 4. The measurement uncertainties of the wood moisture content u are <1% in the dry and fiber-saturated state, and <3% in the maximum saturated state.

Table 3. Summary of curve parameters fitting the wood moisture content u, swelling α, and density d for oak and spruce wood in three measurement directions.

	Fitted u Curve	Corr. Coeff.	Fitted α Curve	Corr. Coeff.	Fitted Density Curve	Corr. Coeff.
Oak wood, in Fiber direction			$10 - 0.05 \times e^{-\frac{u_o}{14.5}}$	0.98		
Across Fiber direction, radial to annual rings	$71.04 + 0.15 \times t - 61.68 \times e^{-\frac{t}{14.12}}$	1	$10.05 - 0.47 \times e^{-\frac{u_o}{30.4}}$	0.98	$0.0047\, u_o + 0.56$	1
Across Fiber direction, tangential to annual rings			$10.14 - 0.52 \times e^{-\frac{u_o}{26.4}}$	0.99		
Spruce wood, in Fiber direction			$10.07 - 0.03 \times e^{-\frac{u_s}{42.9}}$	0.96		
across Fiber direction, radial to annual rings	$94.99 + 0.17 \times t - 80.12 \times e^{-\frac{t}{11.91}}$	1	$10.36 - 0.71 \times e^{-\frac{u_s}{35.5}}$	0.98	$0.0031\, u_s + 0.38$	1
across Fiber direction, tangential to annual rings			$10.45 - 0.7 \times e^{-\frac{u_s}{40.6}}$	0.97		

Table 4. Summary of physical wood properties for oak and spruce wood in the kiln-dry and in the saturated state.

	Spruce Wood Kiln-Dry State (0% Moisture Content)	Spruce Wood Moisturized State (130% Moisture Content)	Oak Wood Kiln-Dry State (0% Moisture)	Oak Wood Moisturized State (100% Moisture Content)
Mass [g]	375.0	867.5	525.5	1055
Density [g/cm^3]	0.39	0.80	0.57	1.04
Volume [cm^3]	955.38	1080.79	923.21	1014.02
Length in fiber [cm] Direction	10.04	10.07	9.95	10.00
Length across fiber direction, radial [cm]	9.70	10.32	9.63	10.02
Length across fiber direction, tangent. [cm]	9.81	10.40	9.63	10.12

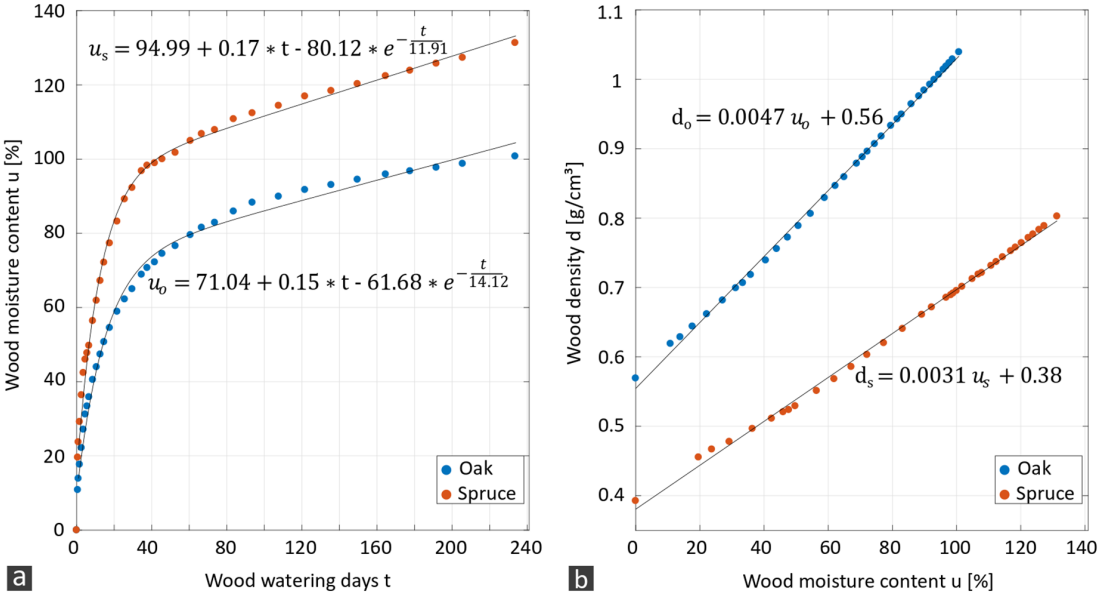

Figure 4. (**a**) Wood moisture content of oak (blue) and spruce wood (red) plotted against the wood watering time in days. (**b**) Development of wood density depending on the wood moisture content for oak (blue) and spruce (red).

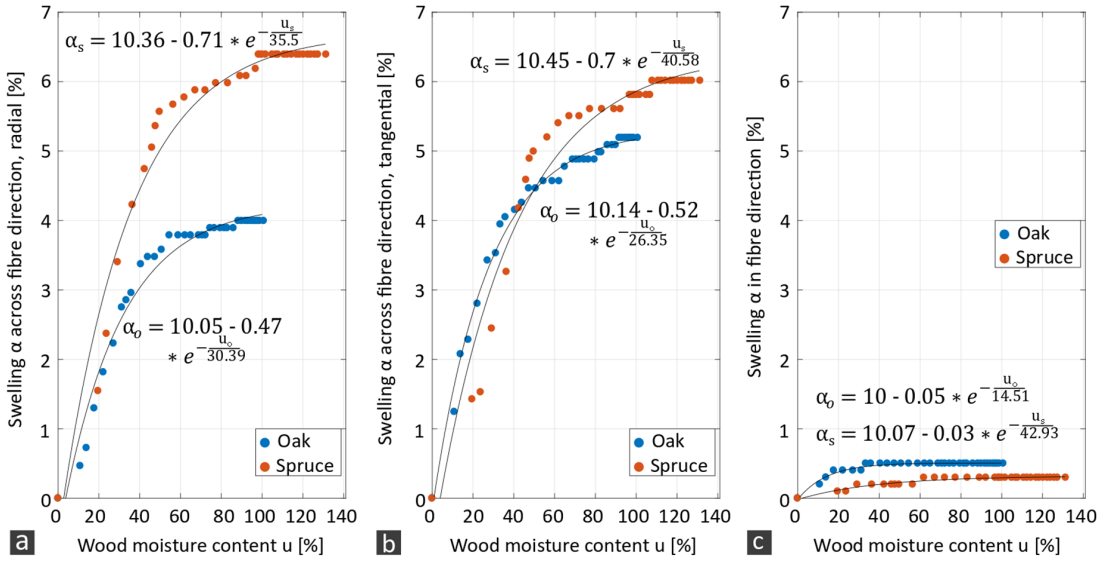

Figure 5. Swelling α of oak (blue) and spruce wood (red) depending on the wood moisture content (**a**) in the direction across the fiber, radial to annual rings, (**b**) in the direction across the fiber, tangential to annual rings, and (**c**) in the fiber direction.

3.2. Electric Resistivity

The results of the measurements of electric resistivity for oak and spruce wood with increasing wood moisture content are presented in Figure 6 and in Table 5. There is a limited exponential decay of the specific resistivity with increasing wood moisture content, for which the fitting functions are given in Table 6. The two wood types and the three main anisotropy directions show distinctly different values. The specific resistivity of oak wood converges to a minimum value of about 250 Ωm, which is also approximated by the asymptotes of the fitted curves. The spruce wood also converges to a minimum resistivity value of about 250 Ωm. For the uncertainties of the derived electric resistivity values, we obtained an almost constant value of <3.5% for all investigated states. The possible effects of

the cube surface boundaries on the geometry factor and thus on the measurements are within the range of the measurement errors and can be neglected. The anisotropy of electric resistivity is largest in the dry state. Measurements in the fiber direction are slightly less resistant compared to the measurements from the direction across the fiber. At higher wood moisture content, the anisotropy effects become smaller. The anisotropy effects of the wood have a maximum of 15%.

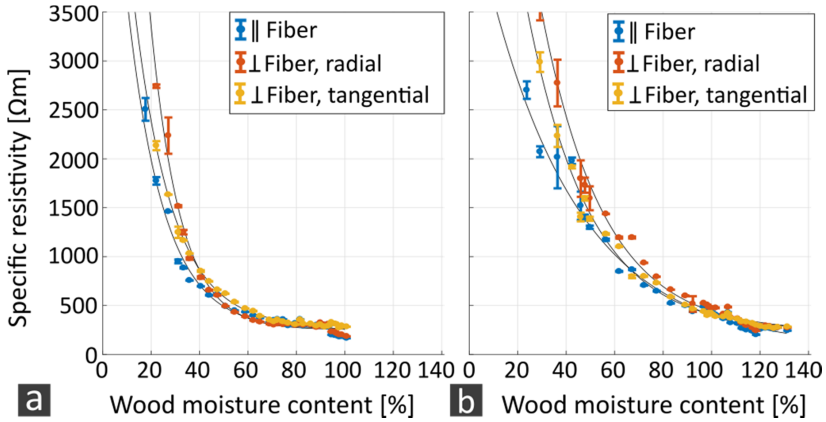

Figure 6. Electric resistivity of (**a**) oak and (**b**) spruce depending on the wood moisture content in the fiber direction (blue error bar), in the direction across the fiber, radial to annual rings (red error bar), and in the direction across the fiber, tangential to annual rings (yellow error bar). The equations of the fitted curves can be found in Table 6.

Table 5. Summary of electric resistivity values for oak and spruce wood in the kiln-dry and in the fully saturated state (extrapolated).

	Spruce Wood Kiln-Dry State (0% Moisture Content)	Spruce Wood Moisturized State (200% Moisture Content)	Oak Wood Kiln-Dry State (0% Moisture)	Oak Wood Moisturized State (111% Moisture Content)
In Fiber direction	>2500 Ωm	79 Ωm	>3500 Ωm	312 Ωm
Across Fiber direction, radial to annual rings	>2500 Ωm	297 Ωm	>3500 Ωm	272 Ωm
Across Fiber direction, tangential to annual rings	>2500 Ωm	270 Ωm	>3500 Ωm	286 Ωm

Table 6. Summary of curve parameters fitting the electric resistivity and dielectric permittivity measurements for oak and spruce wood in three measurement directions.

	ρ_s: Fitted Curve	Corr. Coeff.	ε_r: Fitted Curve	Corr. Coeff.
Oak wood, In Fiber direction	$310.0 + 8068 \times e^{-\frac{u}{13}}$	0.99	$-9.5 + 9.9 \times e^{\frac{u}{85.5}}$	1
Across Fiber direction, radial to annual rings	$270.8 + 16520 \times e^{-\frac{u}{12}}$	0.99	$1 + 1.6 \times e^{\frac{u}{51.8}}$	1
Across Fiber direction, tangential to annual rings	$278.5 + 7549 \times e^{-\frac{u}{16}}$	1	$-7.6 + 9.2 \times e^{\frac{u}{100.9}}$	0.99
Spruce wood, In Fiber direction	$52 + 4578 \times e^{-\frac{u}{39}}$	0.95	$-4.6 + 6 \times e^{\frac{u}{92.9}}$	0.99
Across Fiber direction, radial to annual rings	$294 + 11120 \times e^{-\frac{u}{24}}$	0.87	$1.2 + 1.3 \times e^{\frac{u}{60.5}}$	1
Across Fiber direction, tangential to annual rings	$266.9 + 8592e^{-\frac{u}{25}}$	0.94	$-0.1 + 1.5 \times e^{\frac{u}{55.2}}$	0.98

3.3. Dielectric Permittivity

Figure 7 presents the results of the dielectric permittivity with increasing wood moisture content. Again the wood types oak (Figure 7a) and spruce (Figure 7b) as well as the three anisotropy measurement directions are distinguished. The measurement uncertainties are 5%, 4%, and 2% for the kiln-dry, fiber-saturated, and maximally saturated states, respectively. The offset that results from picking the first maxima of the wavelets (Figure 3b, option 1) instead of the first breaks (Figure 3b, option 2) is about 5% in the dry state and about 20% in maximum saturated state. For oak wood, we found an exponential increase in the relative dielectric permittivity with moisture content (Figure 7 and Table 6). The three measurement directions show a relative dielectric permittivity of ~2 in the kiln-dry state. For the maximally reached wood moisture content in the experiment, the relative dielectric permittivity increases to 12–22 according to fiber direction. The dielectric permittivity values extrapolated to full water saturation are summarized in Table 7. As a result of the unsteady measurement curve for the tangential direction across the fiber of the spruce wood, we used an estimate instead of the extrapolation. The ratio of the three measuring directions at the last measured value was maintained. This suggests that anisotropy effects become larger with increasing wood moisture content. The minimum and maximum permittivity values for all measurement directions of spruce wood are slightly lower than those of the oak. The anisotropy effects of the GPR measurements have a maximum of 30%.

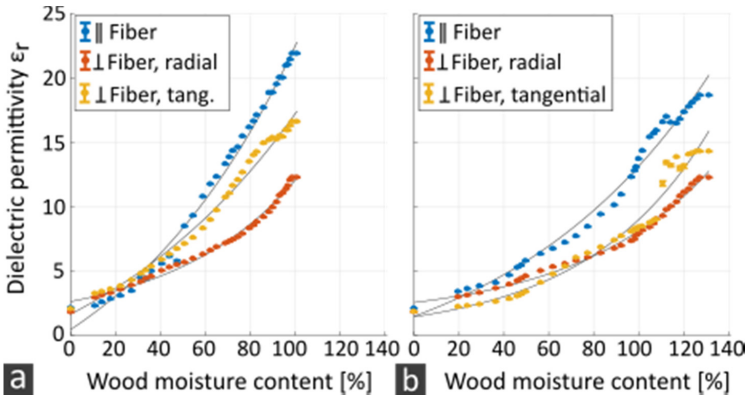

Figure 7. Dielectric permittivity of (**a**) oak and (**b**) spruce depending on the wood moisture content in the fiber direction (blue error bar), in the direction across the fiber, radial to annual rings (red error bar), and in the direction across the fiber, tangential to annual rings (yellow error bar).

Table 7. Summary of dielectric permittivity values for oak and spruce wood in the kiln-dry and in the fully saturated state (extrapolated).

	Spruce Wood Kiln-Dry State (0% Moisture Content)	Spruce Wood Moisturized State (200% Moisture Content)	Oak Wood Kiln-Dry State (0% Moisture)	Oak Wood Moisturized State (111% Moisture Content)
In Fiber direction	1.8	47	2	27
Across Fiber direction, radial to annual rings	1.8	37	2	15
Across Fiber direction, tangential to annual rings	1.8	41	2.1	20

3.4. Relative Material Parameter Contrasts

From the investigations of the electric resistivity and the dielectric permittivity of moisturized wood extrapolated from the experiment, the relative material contrasts of wood in different subsoils could be calculated using additional literature values. Figure 8 and Table 8 summarizes the results, which distinguish between geoelectrical (Wenner α) and GPR material contrasts of wood in fresh water, a clayey subsoil, and a sandy subsoil.

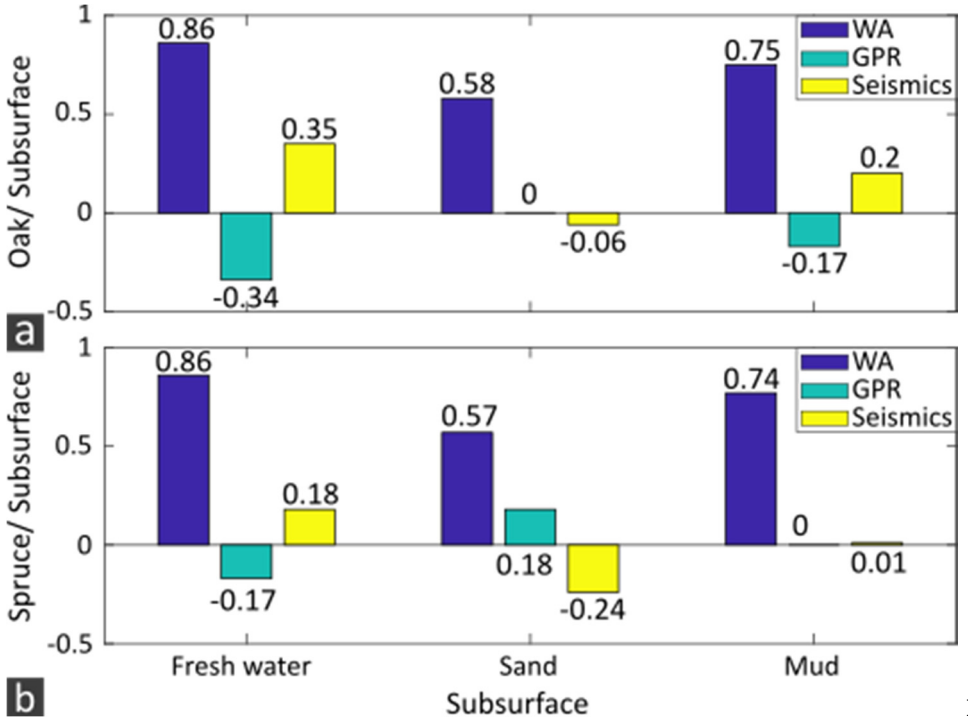

Figure 8. Comparison of relative material contrasts of oak wood (**a**) and spruce wood in tangential the direction across the fiber (**b**) to fresh water (**left**), sandy subsurface (**middle**), and clayey subsurface (**right**) for geoelectrical (Wenner α, blue), ground penetrating radar (GPR) (green), and seismic measurements (yellow).

Table 8. Comparison of the reflection coefficient of unweathered oak and spruce wood with the subsoil and the water column for the following methods: electric resistivity tomography (ERT), GPR, and seismics. For ERT and GPR, the range of material contrasts determined in the radial direction across the fiber (first value) and in the fiber direction (second value) are given. The seismic reflection coefficients were calculated for pine instead of spruce wood.

	ERT	GPR	Seismics
Oak wood compared to fresh water	0.86 to 0.87	−0.4 to −0.27	0.35
Spruce wood compared to fresh water	0.87 to 0.58	−0.19 to −0.14	0.18
Oak wood compared to sandy subsoil	0.56 to 0.61	−0.07 to 0.07	−0.06
Spruce wood compared to sandy subsoil	0.6 to 0.3	0.15 to 0.21	−0.24
Oak wood compared to clayey subsoil	0.74 to 0.77	−0.24 to −0.1	0.2
Spruce wood compared to clayey subsoil	0.76 to 0.33	−0.01 to 0.04	0.01

Figure 8 is based on the tangential direction across the fiber. Table 8 provides the variation of contrasts when additionally considering the fiber direction and the radial direction across the fiber. In addition, relative seismic material contrasts whose physical parameters were taken from [11] are listed. The pine wood used in the study of [11] is listed as spruce wood for reasons of comparability of soft and hard woods. Comparing the three methods, the largest parameter contrasts can be expected for the geoelectric measurements, followed by GPR, and seismic measurements. For all methods, the

highest material contrasts for nonweathered wood can be found in water, followed by a clayey, and sandy subsoil. For both GPR and seismic measurements, there are exceptions where the surrounding materials cause very low contrasts. This applies in particular to the contrast of oak wood compared to a sandy subsoil and of pine wood compared to a clayey subsoil.

3.5. Geophysical Detection Swell of Wooden Targets in Lacustrine Environment

Figure 9a shows the linear relationship between the body diameter and its maximum detection depth for geoelectric measurements. A wooden body of the diameter 0.5 m can be detected at a depth of 0.5–1.5 m. The shape of the body is more important than the surrounding material. The deepest objects can be detected in fresh water, followed by saturated clay and saturated sand. For GPR measurements, an object with a diameter of 0.5 m can be detected at between 0.5 m and 3 m in depth (Figure 9b). The surrounding materials show a stronger influence on the results, whereas the curves for cylinders and spheres are in similar value ranges. The deepest penetration is reached in freshwater, followed by saturated sand. In particular, saturated clay shows a high attenuation.

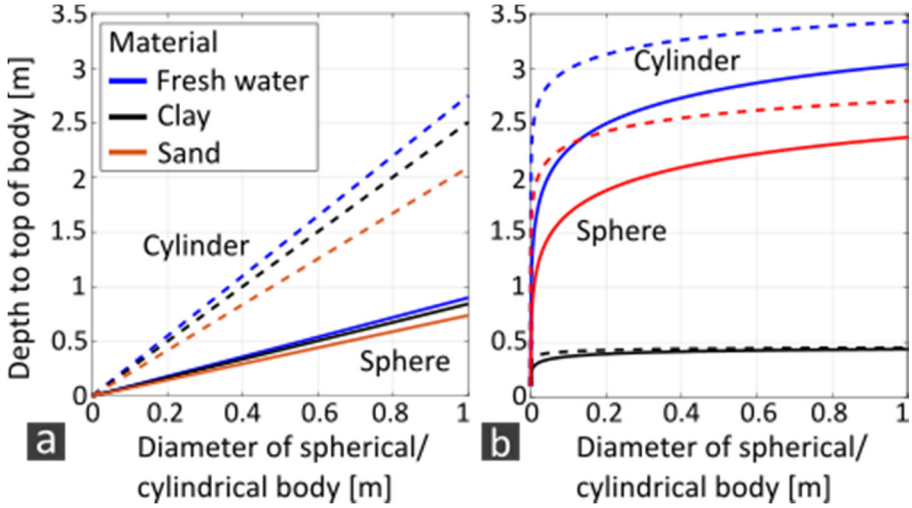

Figure 9. Estimation of the maximum detectable depth position of a spherical (solid line) and cylindrical (dashed line) wooden body as a function of its diameter x. (**a**) Geoelectrical (Schlumberger) and (**b**) GPR investigations (400 MHz) as well as the subsurface materials fresh water (blue line), clay (black line), and sand (red line) are distinguished.

There is a clear difference between the methods. In contrast to geoelectrics, GPR measurements can detect diameters of >10 cm at depths of 0.5–2.75 m. For a 400 MHz antenna and for diameters > 0.5 m, the maximum depth penetration is reached, whereas geoelectrical measurements are not limited here.

4. Discussion

4.1. Swelling and Density Increase of Moisturized Wood during the Experiment

4.1.1. Swelling

The percentage of wood swelling observed in our experiment coincides with studies of [17,19]. They found a linear swelling until the fiber-saturated state was reached (at a wood moisture content of 30% and 23% for spruce and oak wood, respectively). After that, the curve converges to a maximum limit. In our experiment, a linear increase in swelling of the same order was observed, too. The linear swelling was observed until a wood moisture content of 50% and 30% was reached for oak and spruce wood, respectively. These differences can be explained by the irregular water absorption of the wooden cube during the watering process in our experiment. By the time the fiber-saturated state was reached

in the wood core, the edges of the cube showed a higher wood moisture content than the maximum fiber saturation. The maximum swelling limit depends on the anisotropy direction and type of wood. Oak as the denser wood shows the greater swelling. The experimentally determined swelling in the fiber direction fits well with the values from [17] (see also Table 9). However, the internal wood structure of the spruce cube does not allow a clear separation of radial and tangential anisotropy axes in the direction across the fiber for the chosen measurement directions on each side of the wood cubes. Thus, the radial and tangential directions across the fiber show an average value of the reported values in the literature. For oak wood, the swelling in the direction across the fiber remains smaller than presented in [17]. This may have been caused by incomplete wood moisture saturation.

Table 9. Comparison of wood swelling observed during our experiment and from the studies in [17].

Swelling	Experiment	Literature
Spruce, in fiber	0.29%	0.2%–0.4%
Spruce, across fiber, radial	6.4%	3.7%
Spruce, across fiber, tangential	6%	8.5%
Oak, in fiber	0.5%	0.3%–0.6%
Oak, across fiber, Radial	4%	4.6%
Oak, across fiber, Tangential	5.1%	10.9%

4.1.2. Density

Focusing on the average raw density of the woods, [17] reports average values of 0.43 g/cm^3 and 0.63 g/cm^3 for spruce and oak, respectively. The wood cubes used for our laboratory experiment show values of 0.39 g/m^3 and of 0.57 g/m^3 for spruce and oak wood, respectively. Hence, they represent their respective wood types. The observed linear density increase of the wood cubes with increasing wood moisture content during the experiment corresponds to investigations presented in [18].

4.2. Electric Resistivity

4.2.1. Experimental Data

The decrease in the electric resistivity with moisture content in our experiment is in accordance with the studies in [18,19,21]. In [18], the specific resistivity is determined as a function of the moisture content for redwood. The study states that kiln-dry wood is a good isolator and that there is a linear relationship between the logarithm of the specific resistivity and the wood moisture content up to fiber saturation. At fiber saturation, the curve converges towards 80 Ωm. The same trend is also observed in our experiment. A constant decrease in the electric resistivity can be observed until a wood moisture content of 50% for spruce and of 33% for oak was reached. Then, the values converge towards 250 Ωm for both oak and spruce, which could be fitted by exponential decay curves. Deviations of the asymptotes of the fitted curves from the average values of the measurements are within the limits of the measurement inaccuracies of 3%.

4.2.2. Anisotropy

We determined higher anisotropy effects of 15% for experimental measurements in the fiber-saturated state (30% wood moisture content) than at the maximum wood moisture content reached (120% wood moisture content). Here, anisotropy effects of 5% become almost negligible (see also Table 10). A comparable study in [17] investigated the specific electric resistivity in the directions along and across the fiber for a wood moisture content of 9% for copper beech. The significantly higher

observed anisotropy effects of 110% are possibly related to the low wood moisture content of 9% used in the study.

Table 10. Weighting of the influences of measurement errors, wood types, and anisotropy effects on the measured values of electric resistivity and dielectric permittivity.

	Measurement Errors		**Wood Type**		**Anisotropy**	
State	Kiln dry	Wet	Kiln dry	Wet	Kiln dry	Wet
Electric Resistivity	<3%	<2%	30%	15%	15%	5%
Dielectric permittivity	<5%	<5%	3%–19%	3%–19%	7%	32%

4.2.3. Wood Species

We also consider the relative standard deviations of the arithmetical averaged electric resistivity from the two types of wood. In our experiment, differences between the two wood types of 30% were obtained in relatively dry condition (see Table 10). With a maximally reached wood moisture content of 130%, the value decreases to 15%, so that the differences between the wood types become smaller. In order to compare the results with the literature, again a study in [17] was taken into account. Here, deviations of 57% were observed for a wood moisture content of 20%, which are again significantly larger than our experimentally determined values. From this, it can be concluded that there are also large inhomogeneities within a wood species that are caused by age and density differences as well as different parts of the internal trunk structure.

4.3. Dielectric Permittivity

4.3.1. Experimental Data

In our experiment, we could see an increase in dielectric permittivity observed in [24,25]. The dielectric permittivity as a function of the wood moisture content is discussed in detail for spruce wood (in the radial across fiber direction) in [17,24]. The results of [17] are summarized in Table 11. The observed results of our experiment agree with those of the literature. Spruce wood showed higher permittivity values than oak wood (see Table 7) due to its higher reached maximum wood moisture content. In our experiment, the highest permittivity values were obtained in the fiber direction, followed by the tangential and radial direction to the annual rings in the direction across the fiber. This is comparable to the values in [23]. In [26], the dielectric constant in the directions with and across the fibers for kiln-dry spruce and oak wood is also investigated. A permittivity of 3.06 was obtained for spruce in the fiber direction, whereas permittivity values of 1.98 and of 1.91 were obtained for the radial and tangential directions across the fiber. Oak wood shows a dielectric permittivity of 2.86 in the fiber direction, of 2.3 in the radial direction and of 2.46 in the tangential direction across the fiber. In addition to the measurement errors of less than 5%, the deviations compared to the reference literature values are within the scope of the inaccuracy, which is caused by picking the maximum signal amplitude instead of the first break of the signal amplitude. Our results apply to the GHz range. A discussion of the change in permittivity with the measurement frequency is given in [19,24]. The dielectric permittivity of spruce wood in the radial direction at a wood moisture of 96% is about 10 for a measurement frequency of 400 MHz and about 7 for a measurement frequency of 2 GHz [24]. Thus, we expect slightly higher permittivity values for lower measurement frequencies used during field prospections than in the experiment. This also affects the material contrasts. However, our results regarding the resolution of wood in various embedding materials and the influence of wood species and cutting directions on the material contrasts remain unchanged.

Table 11. Comparison of dielectric permittivity values of spruce wood depending on the wood moisture content observed during our experiment and in [17].

Wood Moisture Content	Experiment	Literature
0%	1.8	1.7
30%	3.2	3.5
80%	6.1	7

4.3.2. Anisotropy

In order to derive anisotropy coefficients of hard and soft wood from the literature, which we defined as relative standard deviations between the measured values of the three anisotropic directions, we refer to [23,26]. In [26], they investigated the dielectric permittivity of oak and spruce for the three anisotropy axes of kiln-dry wood. On the basis of these results, we calculated an anisotropy effect of 28% for spruce wood and of 11% for oak wood. Our experimentally measured data shows lower anisotropy effects of 8% for kiln-dry wood (see Table 10). To investigate the anisotropy effects for a wood moisture content of 30%, we considered the study of [23]. Here, the dielectric permittivity was investigated for the three anisotropic directions for pine wood. On the basis of these results, we calculated a relative standard deviation of 27%, which fits well to the anisotropy effects of 20%–37% observed in our experiment.

4.3.3. Wood Species

To investigate the influence of different wood species on the dielectric permittivity with increasing wood moisture content in the literature, we refer to [17,26]. In [26], they investigated the dielectric permittivity for kiln-dry oak and spruce wood in three anisotropy directions. On the basis of these results, we calculated relative standard deviations of 5%–18% depending on the measurement axis. Furthermore, we used [17] to differentiate between deviations of wood species in moisturized state in the fiber direction. For spruce and birch wood, we calculated deviations of 11% for a wood moisture content of 30%, and deviations of 18% for a wood moisture content of 80% from the study. From the dielectric permittivity values observed in our experiment, deviations of 3%–19% (see Table 10) were reached for dry and moisturized wood.

4.4. Relative Material Parameter Contrasts

Our investigations show that GPR and seismic measurements have an equal amount of advantages and disadvantages in the resolution of fresh water-saturated, unweathered wood in different embedding materials. In particular, material contrasts of hardwood compared to sand and softwood compared to clay are difficult to prospect. The wood species and the structural orientation of the wood contribute to whether a wooden objected can be found. For geoelectric measurements, we cannot distinguish between the influences of the wood species and the structural orientation of wood on the material contrasts. This is different with GPR measurements. Here, the type of wood and the structural orientation show different effects on the material contrasts. Moreover, the wood species have a stronger influence on the contrasts than the structural orientation of the wood. The described differences of the measurement methods can be explained by the varying the maximum wood moisture content of the wood species. The electrical resistivity values observed during the experiment did not change significantly for higher saturation rates. The dielectric permittivity, on the other hand, increased proportionally to the maximum wood moisture content of the respective wood species. In this study, we do not consider the effect of weathered wood on the contrasts. Compared to moisturized wood, even lower electric resistivity values and higher dielectric permittivity values are to be expected for weathered wood. Thus, we can assume that material contrasts of weathered wood compared to fresh water become smaller, whereas contrasts compared to a sandy or clayey subsoil might increase. This will also affect the depth range. Therefore, in a freshwater environment, weathered wood can be

prospected at shallower depths than unweathered wood. In a clayey or sandy subsurface, this might be reversed. As a result of the increased material contrasts, weathered wood can possibly be prospected at greater depths than unweathered wood.

4.5. Comparison of Measurement Methods

For geoelectric measurements, sufficient material contrasts can be expected for hard and soft wood compared to all investigated embedding materials regardless of the structural orientation of the wood. With this method, cylindrical objects of diameters > 2 m can be prospected in depths > 3 m. The method is limited to the resolution of objects > 0.5 m for depths of > 0.5 m. However, the method can hardly distinguish between wood species and cutting directions. GPR is suitable for prospecting objects of 10–50 cm diameter in depths of 1–3 m. There are limitations for the depth penetration of clayey soil. Under certain conditions (depending on the wood species, structural orientation of the wood, and embedding materials), material contrasts may be too low to be detected. The method is suitable to distinguish heterogeneities of wood species and structural orientation within an object. Seismic and GPR measurements show similar material contrasts. The major advantage of seismic measurements is the depth penetration in saline water, whereas GPR measurements are unsuccessful in this media. Limitations are possible in very shallow water and in gassy subsurfaces.

5. Conclusions

In our study, we define the scopes of application of geoelectrics and GPR, supplemented by seismics to prospect submerged wooden archaeological objects in a shallow water environment. Therefore, we had to experimentally determine changes in the dielectric permittivity and the electric resistivity of wooden samples for a large range of wood moisture contents. We systematically distinguish hard and soft woods as well as three main measuring axes with small-scale geophysical measurements. The dielectric permittivity increases by 90%, while the electric resistivity decreases by 90% with a 130% change in wood moisture content. When comparing the three main measuring axes, anisotropy effects of up to 30% for dielectric permittivity measurements and up to 15% for electric resistivity measurements occur. Different types of wood also account for a change of up to 20% in dielectric permittivity measurements and up to 30% in the electric resistivity measurements.

The calculated material contrasts from wood compared to the embedding materials (freshwater, saturated clay, and sand) show the potential of the methods to complement each other. ERT generally shows the highest material contrasts. Here, differences in wood species and structural orientation of the wood do not significantly affect the material contrasts. This is different with GPR measurements; here, material contrasts depend on the wood species and the structural orientation of the wood. GPR and seismic measurements show especially low contrasts of oak wood compared to saturated sand and of spruce wood compared to saturated clay. However, seismics is the preferable method in saline water. Depth estimates show that geoelectrics is particularly suitable for cylindrical objects (> 0.8 m in diameter) at depths of > 2 m and in a clayey environment. For spherical objects with diameters < 0.8 m at depths of < 2 m, the GPR prospection of wood embedded in saturated sand and freshwater with a 400 MHz antenna is suitable. In general, wood can be most successfully prospected in freshwater, followed by saturated clay and sand. For further investigations on the prospection of submerged archaeological wood, it will be necessary to calculate the material contrasts of weathered wood.

Author Contributions: Conceptualization, A.F., D.W., T.W. and W.R.; methodology, A.F., D.W., T.W. and W.R.; software, A.F. and W.R.; validation, D.W. and T.W.; formal analysis, A.F.; investigation, A.F.; resources, A.F.; data curation, A.F.; writing—original draft preparation, A.F.; writing—review and editing, D.W., T.W. and W.R.; visualization, A.F., D.W.; supervision, D.W., T.W. and W.R.; project administration, W.R.; funding acquisition, D.W., T.W. and W.R. All authors have read and agreed to the published version of the manuscript.

Funding: The research leading to these results has received funding by the German Research Foundation (DFG) in a project (RA 496/26-2) situated in the frame of the Priority Program 1630 'Harbours from the Roman Period to the Middle Ages' (of Carnap-Bornheim and Kalmring 2011).

Acknowledgments: The authors acknowledge especially support from the student assistant Raphael Kahn with his help during the measurements. Stefan Dreibrodt offered his help using the kiln-drying method for the wood cubes. Special thanks is also dedicated to Thomas Günther (LIAG Hannover) for his support to use the program "pyGIMLi" to calculate the geometry factor of the wood cubes. The carpenter's workshop "Stefan Wolter" provided and cut the wood cubes for free. We acknowledge financial support by DFG within the funding programme Open Access Publizieren.

Conflicts of Interest: The authors declare no conflict of interest. The funders had no role in the design of the study; in the collection, analyses, or interpretation of data; in the writing of the manuscript, or in the decision to publish the results.

References

1. Müller, C.; Woelz, S.; Ersoy, Y.; Boyce, J.; Jokisch, T.; Wendt, G.; Rabbel, W. Ultra-high-resolution marine 2D–3D seismic investigation of the Liman Tepe/Karantina Island archaeological site (Urla/Turkey). *J. Appl. Geophys.* **2009**, *68*, 124–134. [CrossRef]
2. Woelz, S.; Rabbel, W.; Mueller, C. Shear waves in near surface 3D media–SH–wavefield separation, refraction time migration and tomography. *J. Appl. Geophys.* **2009**, *68*, 104–116. [CrossRef]
3. Fediuk, A.; Wilken, D.; Wunderlich, T.; Rabbel, W.; Seeliger, M.; Laufer, E.; Pirson, F. Marine seismic investigation of the ancient Kane harbour bay, Turkey. *Quat. Int.* **2018**, *511*, 43–50. [CrossRef]
4. Seeliger, M.; Brill, D.; Feuser, S.; Bartz, M.; Erkul, E.; Kelterbaum, D.; Vött, A.; Klein, C.; Pirson, F.; Brückner, H. The purpose and age of underwater walls in the Bay of Elaia of Western Turkey: A multidisciplinary approach. *Geoarchaeology* **2014**, *29*, 138–155. [CrossRef]
5. Wunderlich, T.; Wilken, D.; Erkul, E.; Rabbel, W.; Vött, A.; Fischer, P.; Hadler, H.; Heinzelmann, M. The river harbour of Ostia Antica-stratigraphy, extent and harbour infrastructure from combined geophysical measurements and drillings. *Quat. Int.* **2018**, *473*, 55–65. [CrossRef]
6. Simyrdanis, K.; Papadopoulos, N.; Kim, J.H.; Tsourlos, P.; Moffat, I. Archaeological investigations in the shallow seawater environment with electrical resistivity tomography. *Near Surf. Geophys.* **2015**, *13*, 601–611. [CrossRef]
7. McGrail, S. *Ancient Boats in North-West Europe: The Archaeology of Water Transport to AD 1500*; Addison-Wesley Longman, Incorporated: London, UK, 1998.
8. Crumlin-Pedersen, O. Nordic Clinker Construction. In *The Philosophy of Shipbuilding. Conceptual Approaches to the Study of Wooden Ships*; Hocker, F.M., Ward, C., Eds.; Texas A&M University: College Station, TX, USA, 2004; pp. 37–64.
9. Diener, A. *Holzbau in Mittelalter und Neuzeit*; Mitteilungen der Deutschen Gesellschaft für Archäologie des Mittelalters und der Neuzeit: Paderborn, Germany, 2012.
10. Wilken, D.; Wunderlich, T.; Hollmann, H.; Schwardt, M.; Rabbel, W.; Mohr, C.; Schulte-Kortnack, D.; Nakoinz, O.; Enzmann, J.; Jürgens, F.; et al. Imaging a medieval shipwreck with the new PingPong 3D marine reflection seismic system. *Archaeol. Prospect.* **2019**, *26*, 211–223. [CrossRef]
11. Arnott, S.H.; Dix, J.K.; Best, A.I.; Gregory, D.J. Imaging of buried archaeological materials: The reflection properties of archaeological wood. *Mar. Geophys. Res.* **2005**, *26*, 135–144. [CrossRef]
12. Jol, H.M.; Albrecht, A. Searching for submerged lumber with ground penetrating radar: Rib lake, Wisconsin, USA. In Proceedings of the 10th International Conference on Ground Penetrating Radar, Delft, The Netherlands, 21–24 June 2004.
13. Kritikakis, G.S.; Papadopoulos, N.; Simyrdanis, K.; Theodoulou, T. Imaging of Shallow Underwater Ancient Ruins with ERT and Seismic Methods. In Proceedings of the 8th Congress of the Balkan Geophysical Society, Chania, Greece, 5–8 October 2015.
14. Arcone, S.; Finnegan, D.; Boitnott, G. GPR characterization of a lacustrine UXO site. *Geophysics* **2010**, *75*, WA221–WA239. [CrossRef]
15. Ruffell, A. Under-water scene investigation using ground penetrating radar (GPR) in the search for a sunken jet ski, Northern Ireland. *Sci. Justice* **2006**, *46*, 221–230. [CrossRef]
16. Lin, Y.T.; Wu, C.H.; Fratta, D.; Kung, K.J. An integrated acoustic and electromagnetic wave-based technique to estimate subbottom sediment properties in a freshwater environment. *Near Surf. Geophys.* **2010**, *8*, 213–221. [CrossRef]

17. Niemz, P.; Sonderegger, W. *Holzphysik: Physik des Holzes und der Holzwerkstoffe*, 1st ed.; Carl Hanser Verlag GmbH Co KG: München, Germany, 2017.
18. Kollmann, F. *Principles of Wood Science and Technology*; Springer: Berlin/Heidelberg, Germany, 1968.
19. Skaar, C. *Wood-Water Relations*; Springer: Berlin/Heidelberg, Germany, 1988.
20. Stamm, A.J. The Electrical Resistance of Wood as a Measure of Its Moisture Content. *Ind. Eng. Chem.* **1927**, *19*, 1021–1025. [CrossRef]
21. Lin, R.T. A study on the electrical conduction in wood. *For. Prod. J.* **1965**, *15*, 506–514.
22. Kuroda, N.; Tsutsumi, J. Anisotropic behavior of electrical conduction in wood. *Mokuzai Gakkaishi* **1982**, *28*, 25–30.
23. Peyskens, E.; De Pourcq, M.; Stevens, M.; Schalck, J. Dielectric properties of softwood species at microwave frequencies. *Wood Sci. Technol.* **1984**, *18*, 267–280. [CrossRef]
24. Trapp, V.W.; Pungs, L. Einfluß von Temperatur und Feuchte auf das dielektrische Verhalten von Naturholz im großen Frequenzbereich. *Holzforsch. Int. J. Biol. Chem. Phys. Technol. Wood* **1956**, *10*, 144–150. [CrossRef]
25. James, W.L. *Dielectric Properties of Wood and Hardboard: Variation with Temperature, Frequency, Moisture Content, and Grain Orientation (245)*; Department of Agriculture, Forest Service, Forest Products Laboratory: Washington, DC, USA, 1975.
26. Kröner, K.; Pungs, L. Zur dielektrischen Anisotropie des Naturholzes im großen Frequenzbereich. *Holzforsch. Int. J. Biol. Chem. Phys. Technol. Wood* **1952**, *6*, 13–16. [CrossRef]
27. Bartsch, H.J. *Taschenbuch Mathematischer Formeln*; Fachbuchverlag Leipzig im Carl-Hanser-Verlag: Munich, Germany, 2007.
28. Telford, W.M.; Geldart, L.P.; Sheriff, R.E.; Keys, D.A. *Applied Geophysics*; Cambridge University Press: Cambridge, UK, 1990.
29. Rücker, C.; Günther, T.; Wagner, F. pyGIMLi-An Open Source Python Library for Inversion and Modelling in Geophysics. In Proceedings of the 78th EAGE Conference and Exhibition, Vienna, Austria, 30 May–2 June 2016.
30. Butler, D.K. *Near-Surface Geophysics*; Society of Exploration Geophysicists: Tulsa, OK, USA, 2005.
31. Schön, J. *Petrophysik: Physikalische Eigenschaften von Gesteinen und Mineralen*; Akademie-Verlag: Berlin, Germany, 1983.
32. Archie, G.E. The electrical resistivity log as an aid in determining some reservoir characteristics. *Trans. AIME* **1942**, *146*, 54–62. [CrossRef]
33. Annan, P. *Ground Penetrating Radar Principles, Procedures and Applications*; Sensors and Software: Mississauga, ON, Canada, 2003.
34. Knödel, K.; Krummel, H.; Lange, G. *Handbuch zur Erkundung des Untergrundes von Deponien und Altlasten: Band 3: Geophysik*; Springer: Berlin/Heidelberg, Germany, 2013.
35. Davis, J.L.; Annan, A.P. Ground-penetrating radar for high-resolution mapping of soil and rock stratigraphy. *Geophys. Prospect.* **1989**, *37*, 531–551. [CrossRef]
36. Hilterman, F.J. Amplitudes of seismic waves—A quick look. *Geophysics* **1975**, *40*, 745–762. [CrossRef]
37. Töpfer, K. Die Ortung von Störkörpern mit dem Schlumberger-Meßverfahren. *Arch. Meteorol. Geophys. Bioklimatol. Ser. A* **1969**, *18*, 191–220. [CrossRef]